Shaping single crystalline BaTiO 3 nanostructures by focused neon or helium ion milling

I I Olaniyan, S W Schmitt, J Albert, J Garcia Fernandez, Cécile Marcelot, Robin Cours, V Deshpande, N Cherkashin, Sylvie Schamm-Chardon, D J Kim, et al.

PAPER • **OPEN ACCESS**

Shaping single crystalline $BaTiO_3$ nanostructures by focused neon or helium ion milling

To cite this article: I I Olaniyan *et al* 2024 *Nanotechnology* **35** 335301

OPEN ACCESS
IOP Publishing
Nanotechnology

Nanotechnology **35** (2024) 335301 (10pp) https://doi.org/10.1088/1361-6528/ad4713

Shaping single crystalline $BaTiO_3$ nanostructures by focused neon or helium ion milling

I I Olaniyan[1,2], S W Schmitt[1], J Albert[1], J Garcia Fernandez[3], C Marcelot[3], R Cours[3], V Deshpande[1], N Cherkashin[3], S Schamm-Chardon[3], D J Kim[1] and C Dubourdieu[1,2,*]

[1] Helmholtz-Zentrum Berlin für Materialien und Energie, Hahn-Meitner Platz 1, D-14109 Berlin, Germany
[2] Freie Universität Berlin, Physical and Theoretical Chemistry, Arnimallee 22, D-14195 Berlin, Germany
[3] CEMES-CNRS and Université de Toulouse, 29 rue Jeanne Marvig, F-31055 Toulouse, France

E-mail: catherine.dubourdieu@helmholtz-berlin.de

Received 19 February 2024, revised 21 April 2024
Accepted for publication 3 May 2024
Published 28 May 2024

Abstract

The realization of perovskite oxide nanostructures with controlled shape and dimensions remains a challenge. Here, we investigate the use of helium and neon focused ion beam (FIB) milling in an ion microscope to fabricate $BaTiO_3$ nanopillars of sub-500 nm in diameter starting from $BaTiO_3$ (001) single crystals. Irradiation of $BaTiO_3$ with He ions induces the formation of nanobubbles inside the material, eventually leading to surface swelling and blistering. Ne-FIB is shown to be suitable for milling without inducing surface swelling. The resulting structures are defect-free single crystal nanopillars, which are enveloped, on the top and lateral sidewalls, by a point defect-rich crystalline region and an outer Ne-rich amorphous layer. The amorphous layer can be selectively etched by dipping in diluted HF. The geometry and beam-induced damage of the milled nanopillars depend strongly on the patterning parameters and can be well controlled. Ne ion milling is shown to be an effective method to rapidly prototype $BaTiO_3$ crystalline nanostructures.

Supplementary material for this article is available online

Keywords: He ions, Ne ions, focused ion beam, ion milling, helium ion microscope, $BaTiO_3$, nanopillars

1. Introduction

Ferroelectric thin films have an enormous potential for applications in nonvolatile memory devices with low power consumption. In this perspective, they should have the ability to retain a switchable polarization at low dimensions [1–5]. As the surface to volume ratio increases at low dimensions, the interaction of ferroelectricity and ferroionicity becomes more significant [6, 7]. In the past ten years, size reduction and confinement in ferroelectric perovskite nanostructures and superlattices have been shown to induce a variety of exotic polar textures such as flux closures [8], bubbles [9], vortices [10], or skyrmions [11]. Peculiar polar textures and exciting physical properties such as multistate memory, negative capacitance and controllable skyrmion chirality have been predicted to occur in ferroelectric perovskite nanostructures such as nanocylinders [2, 12–14]. One of the challenges for an experimental demonstration of these properties is the fabrication of such ferroelectric nanostructures.

Focused ion beam (FIB) milling is a powerful machining tool offering good precision, rapid prototyping, and operability on the surface of various solid materials [15–17]. Ga-FIB milling has been used extensively in the downscaling of

* Author to whom any correspondence should be addressed.

ferroelectrics and, currently, most studies on fundamental ferroelectric size effects in capacitors [18–20], nanoribbons and lamellae [8, 21–24] rely on this technique. Solutions to eliminate FIB-induced surface damage and Ga ion implantation have been reported [25–27]. He or Ne ion millings have been comparatively less investigated for the fabrication of nanostructures, although He and Ne ion beams can have a spot size as low as 0.5 nm, and 1.9 nm, respectively, while Ga-FIB has a spot size of typically 3 nm [28, 29]. In addition, the low atomic weight of He and Ne ions reduces their scattering cross sections. As a consequence, He and Ne ion milling may result in a lower but more precise milling yield. So far, He ion machining has been used for the fabrication of a variety of nanostructures such as sub-10 nm nanopores in 2D materials [30, 31] or in SiN membranes [32], nanocones patterned from Si [33], graphene resonators [34], or plasmonic dipole nanoantennas with gap values in the range of few nm [35]. As for oxide nanostructures, there are only very few realizations, mainly for high-T_c cuprate nanoconstriction devices [36]. Ne ion milling has been reported for semiconductors [37, 38] and polymer films [39]. The comparison of Ga and Ne ion milled lamellae suggested that both ions induced almost the same damage, but the Ne ion enabled more precise milling of the lamella [40]. To the best of our knowledge, no work on the fabrication of ferroelectric perovskite nanostructures using He or Ne ions has been published. More generally, He and Ne milling bear huge potential for the fabrication of diverse functional oxides nanostructures with a large variety of properties (magnetic, dielectric, piezoelectric, ferroelectric, multiferroic, superconducting…).

In this study, we investigate the nanofabrication of structures shaped in single crystalline $BaTiO_3$ using He and Ne ion milling. We examine the impact of different ion beam energies (in the range of 15–30 keV) and fluences on the sputtering rate and the damage depth. We focus on the realization of nanopillars. The effect of milling sequence on pillar geometry and damage is investigated. We identify the milling and the patterning parameters that allow to reduce surface damage and increase the geometric fidelity of the pillars. We propose a wet etching to remove the amorphized region after the milling procedure. Ne ion milling is shown to be a powerful method for the fabrication of nanostructures with high precision and flexibility.

2. Experimental and simulation methods

2.1. Fabrication of the nanopillars by He or Ne focused ion milling

We used commercial $BaTiO_3$ (001) single crystals (from MaTeK) in this work. A ZEISS Orion NanoFab helium ion microscope (HIM), in which Ne is also available as the source gas, was used for FIB milling. The He or Ne ion beam is created from an electrically biased tungsten tip placed in He or Ne gas at a low pressure of 2×10^{-6} Torr. The nominal beam size of the He and Ne ions is 0.7 nm and 2.5 nm, respectively. Before loading a single crystal into the HIM chamber, it was ultra-sonicated in acetone for 3 min, followed by 5 min cleaning in isopropanol. For beam control and experimental automatization, we used the software 'Nano Patterning and Visualization Engine' (NPVE) provided by Fibics Incorporated. It has two patterning modes, ring converted to polygon patterning style and ring patterning style (RPS). For our experiments, we chose RPS because the ring converted to polygon one leads to an asymmetric distribution of amorphous or damaged regions in the nanopillars. The RPS is divided into three patterning styles depending on how the ion beam moves relative to the desired nanostructure: (1) in-out RPS, (2) out-in RPS, and (3) alternating RPS, as illustrated in figure S1 of the supplementary materials. The dwell time (t_d), beam spacing ($S_{P/R}$), and beam repetitions (N_S) are the parameters controlling the beam fluence. Keeping constant one of these parameters, we varied the two other ones to achieve a constant fluence. The equation for calculating the fluence is given and explained in the supplementary materials (equation S1).

For the He-FIB milling study, circular areas with a radius of 250 nm on the $BaTiO_3$ single crystal were irradiated using various fluences (in the range 2–300 $\times$ 10^{18} ions cm^{-2}) at beam energies of 15 and 30 keV and at a beam current of ~5 pA. For the Ne-FIB milling tests, circular areas with the same radius of 250 nm were irradiated with fluences in the range 9–30 $\times$ 10^{17} ions cm^{-2} at beam energies of 15, 20 and 25 keV and a beam current of 2.5–3.5 pA. To optimize the Ne-FIB milling parameters, we milled cylindrical nanopillars (diameter of ~500 nm) by employing the alternating RPS with beam energies of 15, 20, and 25 keV and beam currents ranging from 2.5 to 3.5 pA. After the optimization, cylindrical $BaTiO_3$ nanopillars of ~ sub-300 nm dimensions were fabricated at a beam energy of 15 keV using the three available scan styles. The parameters used in milling are shown in table S1 of the supplementary materials. Since the usage of alternating RPS results in an effective irradiation twice as much as that of in–out or out–in RPS, the number of scans was reduced by a factor of two for a direct comparison of the different milling modes at equal doses.

2.2. Characterization of the nanopillars

The nanopillars were imaged by scanning electron microscopy (SEM) using a ZEISS Merlin microscope. For cross sectional images, Ga FIB was used to cut the nanopillars (ZEISS Dual CrossBeam340). To protect the nanopillars, carbon (30 nm) was deposited via sputtering and a layer of Pt (400 nm) was deposited by ion beam deposition. The topography of the nanopillars was investigated by atomic force microscopy (Park Systems NX10) in contact mode with the tip (Multi 75Al-G). Confocal Raman spectroscopy (Horiba LabRam) was performed on the as-received and on the nanostructured single crystals using a laser of 325 nm wavelength. High-resolution transmission electron microscopy (HRTEM) was carried out using a Hitachi HF-3300 TEM equipped with a 300 kV cold-field emission gun, a CEOS image aberration corrector and a Gatan OneView 4k $\times$ 4k camera. Cross-section lamellae were prepared using FIB-SEM Thermo Fisher Helios NanoLab 600i. The surface of the

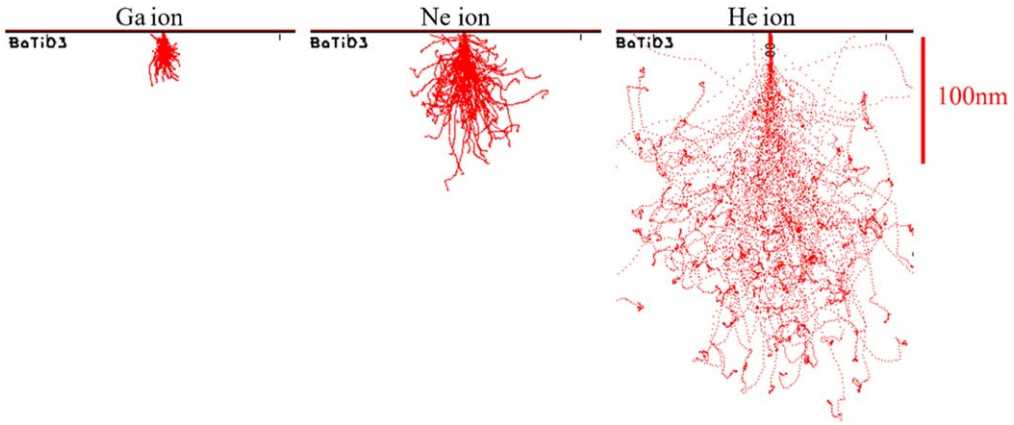

Figure 1. Monte Carlo simulations of 3000 Ga, Ne, and He ion trajectories at 30 keV in single crystalline $BaTiO_3$.

sample was protected with three different layers, one of carbon and two of platinum. The first carbon layer was deposited locally on top of the pillars by focused electron beam-induced deposition (FEBID) as a marker to help locate their position. Then, a ~200 nm thick Pt layer was deposited locally by FEBID and a final ~1.5 μm thick Pt layer was deposited on top using FIB-induced deposition. A micrometer-size lamella containing the pillars was then cut by Ga-FIB, lifted out from the bulk using a micromanipulator, attached to a 3 mm copper grid using Pt ion beam induced deposition and thinned to electron transparency with Ga ions. In the last steps of the thinning process, the energy of the ion beam was gradually decreased from 30 to 2 kV to minimize surface damage. Lamellae were prepared along the [010] crystallographic direction of $BaTiO_3$.

2.3. Monte Carlo simulations

Simulations of the ion penetration depth and their lateral scattering range inside single crystalline $BaTiO_3$ were performed using the binary collision Monte Carlo program 'Stopping and Range of Ions in Matter' (SRIM), version 2013 [41].

Figure 1 highlights the strong differences in the ion-solid interaction volume between Ga FIB as compared to He and Ne FIB milling. Monte Carlo simulations were performed for 3000 ions (Ga, Ne, and He ions) incident on a $BaTiO_3$ single crystal. The heavier the ion, the higher its scattering cross section. Ga ions lose their energy closer to the surface and therefore their interactions are confined near it whereas both the lateral and depth dimensions of the interacting regions of Ne and He ions extend further into the material. The Monte Carlo simulations indicate milling rates of 8.4 atoms/ion, 3.6 atoms/ion, and 0.1 atoms/ion for Ga, Ne, and He ions, respectively. With lighter ions, a slower and, therefore, more accurate milling can be achieved.

3. He ion milling

Thirty areas of a $BaTiO_3$ (001) single crystal, separated from each other by more than 1 μm to avoid cross effects, were irradiated with different He ion fluences at beam energies of 15 and 30 keV. Figure 2(a) shows that, instead of milling, swelling of the surface occurs and eventually surface blistering as the He dose increases (30 keV). Similar observations were made when irradiating the crystal with He ions of 15 keV energy.

AFM topography was recorded to estimate the volume change as a function of fluence (figure 2(b)). The dependence of the swelling volume as a function of He ion fluence can be divided into three regions (figure 2(c)). In the first region, the swelling volume increases linearly with the fluence and is found to be energy independent. Then, starting at a fluence of $\sim 25 \times 10^{18}$ ions cm^{-2}, the linear dependence is still observed but with a smaller slope and seems energy independent as well (region II in figure 2(c)). Finally, in the third region, the swelling volume levels off to a plateau region, for which the volume does not further increase with dosing. These three regimes were also observed in case of He-FIB irradiation (15, 25 and 35 keV incident energies) of 200 nm thick Au {111} films on glass substrates in an ORION NanoFab HIM [42]. However, in metals, the second linear region corresponds to a regime where the volume expansion accelerates (larger slope than in the first linear regime), whereas for $BaTiO_3$, we observe a deceleration of the volume expansion. A similar behavior was observed for Ga_2O_3 under He ion irradiation [43]. Swelling and surface blistering following He ion irradiation have been reported for many materials such as metals (niobium [44], gold [42], and copper [45]), nitrides [32, 46] and semiconductors like Si [47]. These phenomena are related to the formation of He bubbles and cavities as originally explained by Evans [48]. Defects such as vacancies and dislocations are formed under He ion irradiation [49]. At low fluences, He atoms can occupy interstitial positions in the crystal; a further increase in ion fluence leads first to the formation of He nanobubbles, then to an agglomeration of the bubbles forming a cavity. Beyond a certain cavity size, due to the high pressure exerted on the walls by the He gas, the cavity bursts (fissures form) to relieve the excess pressure. Once the fissures reach the surface, the volume of the cavities saturates and further He dosing does not result into an increase in volume (see a scheme in the supplementary materials figure S2). The second linear region of the plot ends

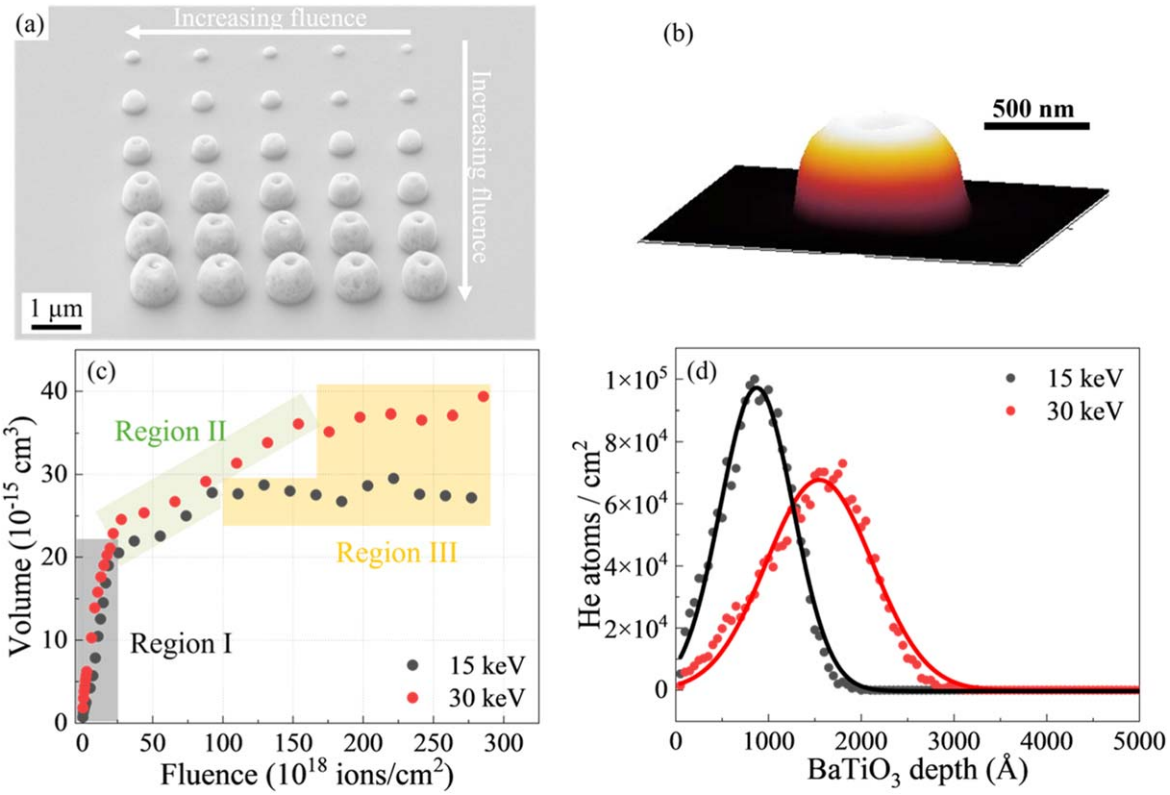

Figure 2. $BaTiO_3$ (001) single crystal irradiated under He ion beam. (a) SEM image of surface swelling in the regions irradiated with different fluences at 30 keV beam energy. The fluence was increased from right to left and from top to bottom as indicated by the arrow. (b) 3D AFM image of the swelling caused by He ion irradiation at a fluence of 10.98×10^{18} ions cm^{-2}. (c) Volume of the surface swelling as a function of the incident He beam fluence at an energy of 15 and 30 keV. (d) Distribution of He implantation as a function of depth using the SRIM simulation of 105 He ions incident on $BaTiO_3$. The dots are the simulated data, and the lines are the Gaussian fits.

at a higher fluence for higher ion energies. Indeed, the 30 keV He ions penetrate deeper into the $BaTiO_3$ and, therefore, more ions are needed for the fissures to propagate and reach the surface; the cavities can grow larger when the beam energy is higher. The depth distribution of He implantation calculated for the two beam incident energies is shown in figure 2(d). It follows a gaussian distribution with a maximum of He atom implantation at ∼90 nm and ∼160 nm below the surface for 15 and 30 keV, respectively. The bubble formation initiates from the region where the He ion implantation is maximum [50].

Since the milling rate of $BaTiO_3$ with He ions is low, high doses are required for milling away tens of nanometer of $BaTiO_3$, which leads to the material swelling and eventually to blistering. Hence, He ions are not suitable for fabricating nanostructures of $BaTiO_3$. It can, however, be used for fine polishing a nanostructure after Ne ion milling.

4. Ne ion milling

4.1. Sputtering yield

Milling rates of Ne ions on $BaTiO_3$ (001) were determined by irradiating at normal incidence a $BaTiO_3$ single crystal at different fluences over regions of 500 nm in diameter. The same experiments were repeated for beam energies of 15, 20 and 25 keV. The milled regions were observed by cross-section SEM images as shown in figure 3(a) (the lamella preparation by Ga-FIB was performed with Pt coverage to avoid damage of the nanostructures by Ga ions). Damage of the subsurface region is observed, corresponding to the amorphization of $BaTiO_3$, which is a typical consequence of ion bombardment on a crystalline material [40, 51]. The milled depth as a function of fluence is presented in figures 3(b), (c). Irrespective of the beam energy, the milled depth increases quasi-linearly with the Ne ion fluence, which provides a precise control of the milling. Milling yields are calculated to be 17, 21 and 14 Å^3/ion for 15, 20 and 25 keV, respectively. The milling rate first increases with increasing energy (with a maximum value at 20 keV) and then decreases for the highest energy of 25 keV. The dependence of milling rates on beam energy (for a given beam fluence) can be understood by considering that there are two counteracting phenomena. On the one hand, the larger the energy is, the more momentum can be transferred to kick out atoms from the material. On the other hand, the ion energy deposited near the surface is a critical parameter for the material ablation. Slower ions loose more of their energy close to the surface while energetic ones (25 keV) do deeper away from the surface. As a result of these two counteracting phenomena, the milling rate for higher ion energies (25 keV here) is lower than that for 15 and 20 keV.

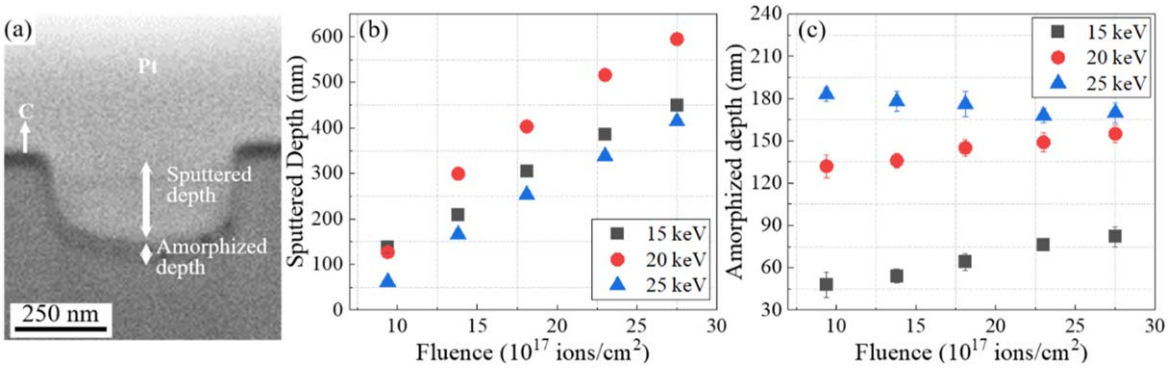

Figure 3. (a) SEM image showing the sputtered depth in a $BaTiO_3$ single crystal milled using Ne ions. The arrows indicate the milled and damaged depths. (b) Sputtered depth as a function of Ne ion beam fluence. (c) Depth of the amorphized region as a function of Ne ion fluence.

Table 1. Dimensions of the amorphous layer and of the pores in the nanopillars fabricated by focused Ne ion beam in an alternating ring patterning scan mode at different beam energies.

Neon beam energy (keV)	Amorphous layer			Size of nanopores (nm)
	On the top of the nano-pillar (nm)	On the side of the nano-pillar (nm)	Outside the nano-pillar (nm)	
15	55	50	85	5–20 nm
20	65	55	130	10–45 nm
25	75	65	160	10–85 nm

Now let us consider the amorphization caused by the milling. In figure 3(c), the subsurface damage depth measured from the cross-section SEM images is plotted as a function of the ion fluence for the three different ion energies. The larger the energy, the larger the amorphized region. The depth of the subsurface damage caused by a beam energy of 25 keV is ~2.5 times larger than that of 15 keV. For 15 and 20 keV, the depth of the damaged layer increases with fluence, which is consistent with previous studies [52]. We observe an opposite trend for 25 keV, likely because the implanted ions are distributed over a wider region beneath the surface.

For high precision milling and for minimizing the potential damages, it is desirable to have both a low milling rate and a low incident energy of 15 keV. This is discussed further in the next section.

4.2. Ne ion milling of nanopillars

Nanopillars of ~500 nm in diameter and ~450 nm in height were fabricated using the alternating ring patterning scan (RPS) mode at different beam energies and a fluence of 11×10^{17} ions cm^{-2}. As shown by the SEM images in figures 4(a)–(c), pores are observed in the milled regions, especially for the 20 and 25 keV energies. They may originate from the coalescence and bursting of Ne bubbles below the surface of $BaTiO_3$. The cross-section images of these pillars are shown in figures 4(d)–(f). For 20 keV, closer views of the regions marked in figure 4(g) and fast Fourier transform (FFT) patterns are given in figures 4(h)–(i).

An amorphous layer surrounds the nanostructures at the top and on the sides, which is confirmed by the ring pattern in the FFT patterns. Embedded within the amorphous layer are nanobubbles, which likely correspond to the agglomeration of Ne atoms and, when reaching the surface, create pores as seen on the SEM images. The Ne ions were directed outside the pillar region to mill around it. The presence of an amorphous region on the sidewalls and top of the pillars is due to lateral and backscattered ions [53]. This effect is typical for ion irradiation and has been also observed for Ga ions milling [54]. Below the amorphized region is a defective region. The extent of the amorphous and defective regions increases with increasing beam energy (see table 1). The single crystalline nature of $BaTiO_3$ is preserved inside the pillar as shown by the FFT patterns. On the side around the pillars, where the Ne ions were directed, a thick amorphous layer has been formed and its thickness increases with beam energy, which is consistent with the previous observations (figures 3(a) and (c)).

The confocal Raman spectra recorded on the regions where the nanopillars were prepared are significantly different from those recorded on the reference single crystal (figure 4(j)). We observe in the nanopillar regions a reduction in the intensity of the E(LO+TO) + B_1(TO) mode peaks at 301 cm^{-1}, the occurrence of the $A_1(TO_3)$ mode peak at 520 cm^{-1}, and an increase in the peak width of the E(LO_4) mode at 722 cm^{-1}. The evolution in the E(LO+TO) + B_1(TO) mode intensity shown in figure 4(k) indicates a reduced tetragonality [55] in the nanopillars as the beam energy increases. The simultaneously increasing peak width of the E(LO_4) mode shows that the distribution of bond lengths becomes larger as higher beam energies are used. The $A_1(TO_3)$ mode is associated with *a*-oriented $BaTiO_3$ domains (in *a*-domains, the long *c* axis of the tetragonal cell lies

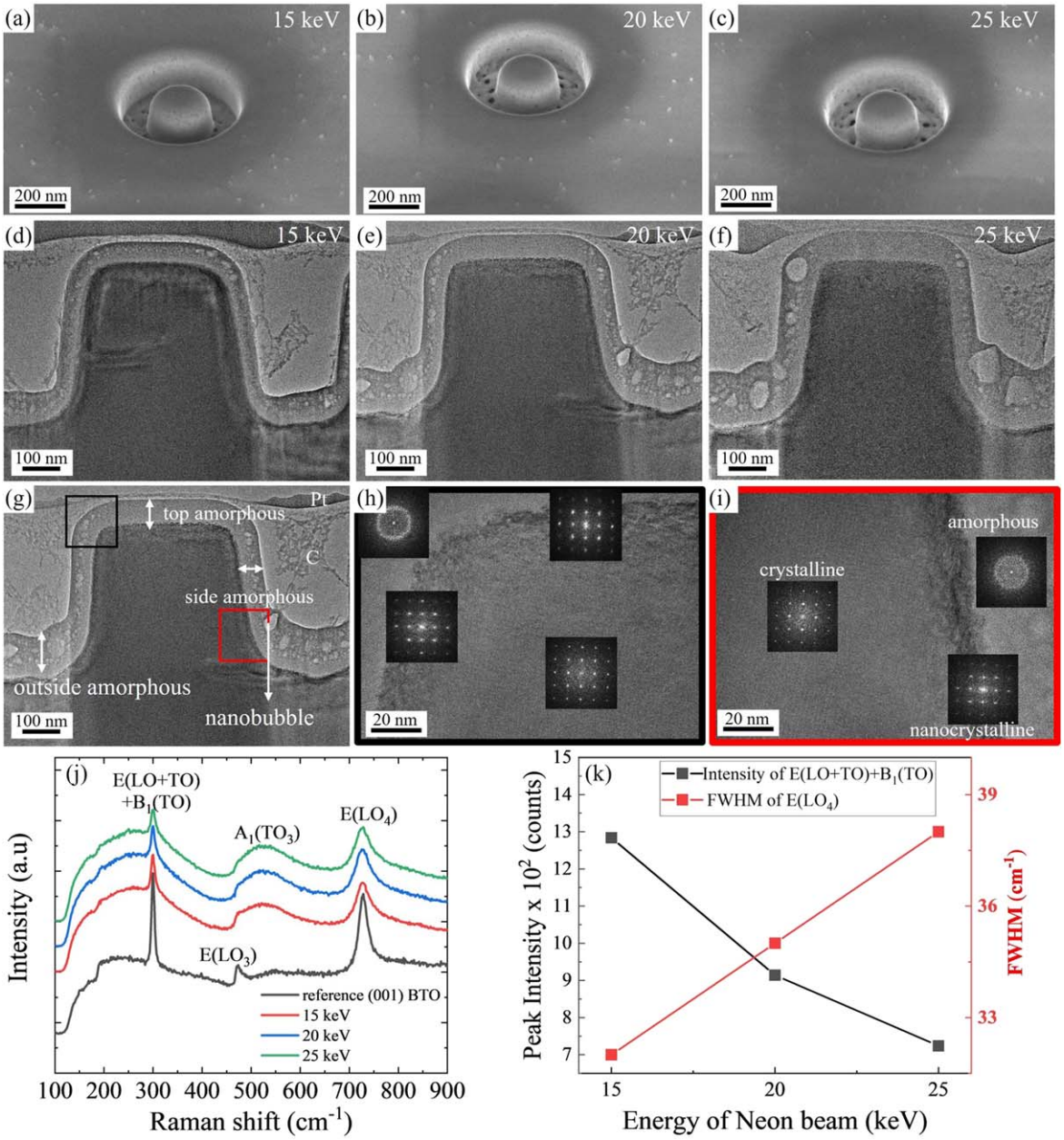

Figure 4. Nanopillars (diameter ∼500 nm) fabricated using focused Ne ion beam at 15, 20 and 25 keV using an alternating ring patterning scan mode. (a)–(c) SEM images of nanopillars fabricated with different energies. (d)–(f) TEM images of nanopillars fabricated with different energies. (g) TEM image of a nanostructure fabricated at 20 keV, indicating different features in the nanostructure and the two regions studied to a higher magnification (h) focus on the top left of the pillar and fast Fourier transform (FFT) patterns of different 20 × 20 nm^2 regions. (i) Focus on the bottom right of the pillar and FFT patterns of different 20 × 20 nm^2 regions. (j) Raman spectra of nanopillars fabricated with different beam energies and compared to the spectrum recorded on the non-milled single crystalline $BaTiO_3$. (k) Peak intensity of the B_1(TO) mode and peak width of the E(LO_4) mode as a function of the beam energy.

in-plane while in *c*-domains, it is perpendicular to the surface) [56, 57]. The area of the $A_1(TO_3)$ peak increases with increasing energy, indicating an increased portion of *a*-domains relative to *c*-domains [56, 57], which originates from the conversion of *c*- to *a*-domains (figure S3 of the supplementary materials). Note that Raman spectra of nanopillars fabricated on a (100) $BaTiO_3$ single crystal (*a*-oriented single crystal) indicate that *c*-domains are present in the nanopillars (originating from the conversion of *a*- to *c*-domains), as shown in figure S4. Recent studies showed that He ions implantation into ferroelectrics can be used to control the out-of-plane strain [58–60], while keeping the in-plane strain unchanged due to the substrate clamping. Guo *et al* [59] reported an increase in the *c* lattice parameter with increasing He ion dose into $La_{0.7}Sr_{0.3}MnO_3$ thin film grown on $SrTiO_3$. A complete disappearance of the in-plane component of the polarization by implantation of He ions into $BiFeO_3$ thin film grown on $LaAlO_3$ was also reported by Herkoltz *et al* [60]. In our case, because there is no clamping of the $BaTiO_3$ crystal from the sidewall of the pillar, Ne ions modify both *c*- and *a*-

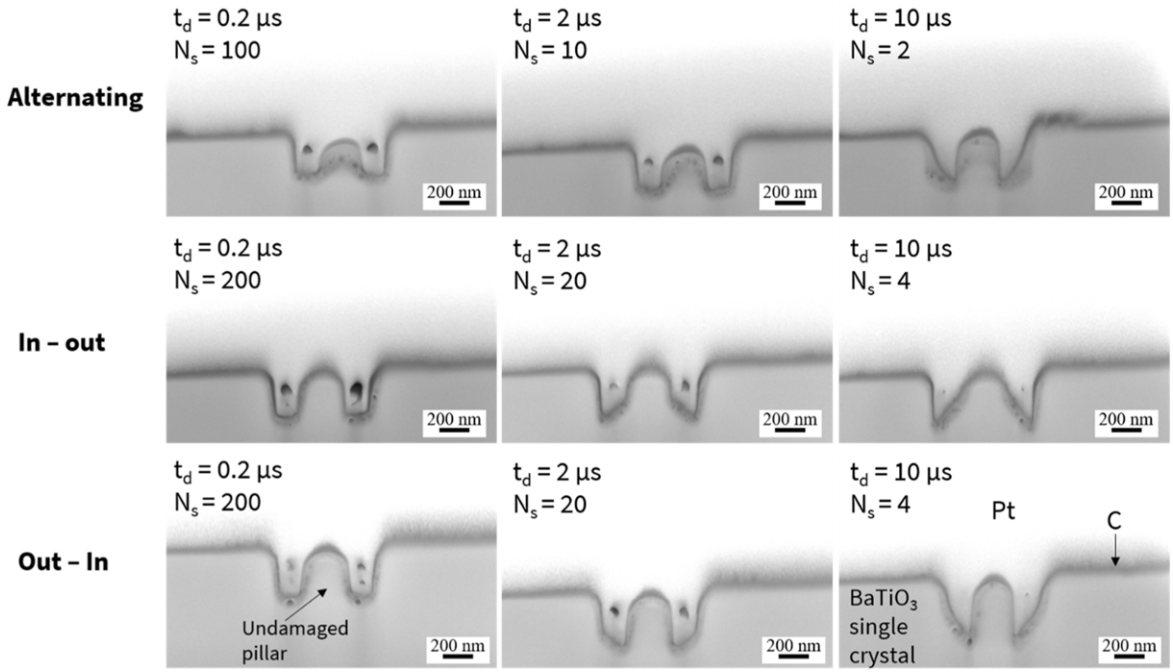

Figure 5. Cross-section SEM images of nanopillars showing the effect of beam dwell time and beam repetition number on the pillar shape. The bright contrast on the top of the images is from the Pt layer which was used as a hard mask during the cross-sectional cut and the dark line surrounding the nanostructures is from C layer deposited before Pt for protection (indicated on the bottom right image).

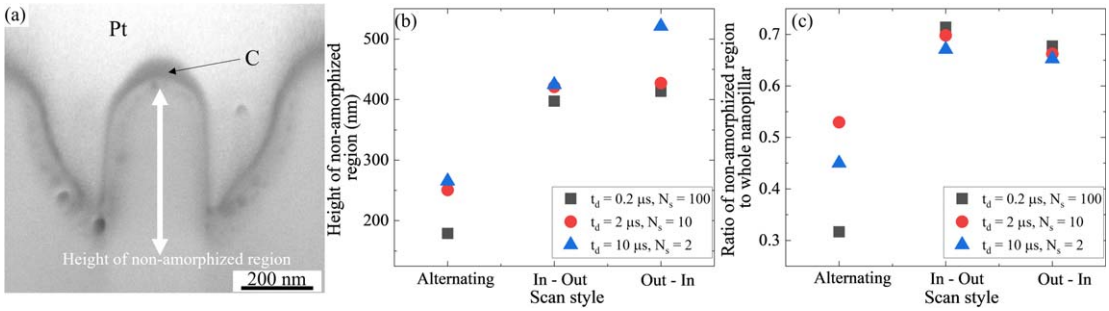

Figure 6. (a) Typical SEM image of a nanopillar milled using an energy of 15 keV. (b) Height of the non-amorphized region for the different processing parameters and repetition scan styles. (c) Ratio of the non-amorphized region area to the whole pillar area for the different processing parameters and repetition scan styles.

domains into *a*- and *c*-domains, respectively. The lowest beam energy (15 keV) gives the smallest peak width of $E(LO_4)$, the highest intensity of $B_1(TO)$ and the lowest area of the $A_1(TO_3)$ peak. Accordingly, the 15 keV beam energy (the lowest energy giving a stable Ne ion beam) is the most suitable for achieving milling with minimized damage and lowest domain mixing in the $BaTiO_3$ nanopillars.

The effects of the dwell time t_d and beam repetition number N_s were studied on nanopillars of diameter ∼300 nm fabricated with a beam current of ∼2.7 pA at a constant beam spacing $S_P/_R$ of 0.25 nm. As explained in the experimental section, alternating RPS effectively deploys a twofold dose on the surface. Accordingly, the number of scans was reduced to one half in order to compare the results with the ones of the unidirectional RPS. The top-view SEM images are shown in figure S5 of the supplementary materials and the cross-view SEM images in figure 5. Figure 6(a) shows a close view of one pillar. As already observed in TEM, there is an obvious damaged region on the side and top of the pillar (consisting of amorphized and nanocrystalline $BaTiO_3$). The shape of the pillars and the extent of the damage depend strongly on the scan style, and for a given one, on t_d and N_s. The alternating RPS clearly leads to a strong amorphization of the top and sidewalls of the pillars (figure 5). For the in-out RPS, a decrease of the beam repetition number N_s results in crown-shaped pillars. The out-in RPS gives a cylindrical shape for all the milling parameters used. The evolution in the shape of the nanopillars is shown in figure S6 of the supplementary materials.

From the cross-section SEM images, we quantified the damage induced by the milling inside the pillars. We define the non-amorphized pillar region (the crystalline and nanocrystalline regions as evidenced in the TEM) as the region with the same contrast in the SEM cross sectional images as

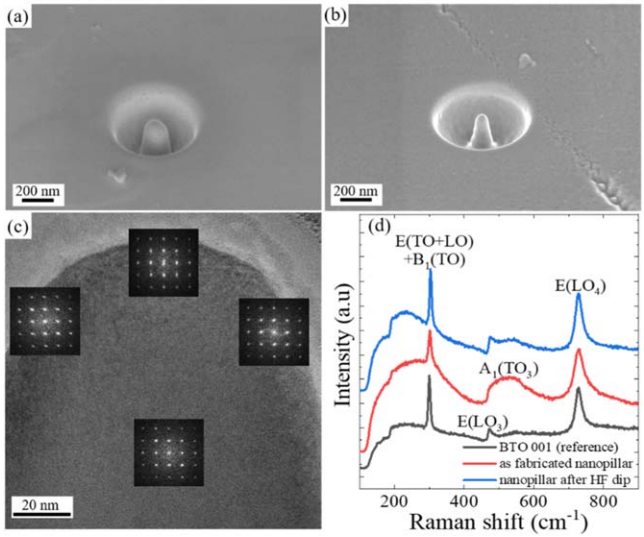

Figure 7. (a) SEM image of a nanopillar before HF dip. (b) SEM image of a nanopillar after HF dip. (c) High-resolution cross-sectional (010) TEM image with focus on the top of the HF dipped nanopillar. (d) Raman spectra of a (001) $BaTiO_3$ single crystal, as fabricated nanopillar, and HF dipped nanopillar.

the non-milled regions (figure S7 of the supplementary materials). The resulting analysis is shown in figures 6(b) and (c) for the different milling conditions. Even though a constant fluence of 12×10^{17} ions cm^{-2} was used, the height and area of the crystalline $BaTiO_3$ pillars are different for variations in patterning style, dwell time t_d and beam repetition number N_s. The out-in RPS mode gives similar height and ratio of non-amorphized material than the in-out RPS but, in addition, preserves the cylindrical geometry of the pillar (figure S6). This patterning style is the optimum one.

To remove the amorphous shell formed by milling, we dipped the nanopillars in a 1% HF solution for 2 min. The SEM images before and after the dip show that the diameter (300 nm at the top and 460 nm at the bottom of the pillar) is reduced by a factor of about 2 after the HF dip (figures 7(a) and (b)). The amorphous phase appears fully etched out, which is confirmed by the FFT patterns performed on different regions of the top and sidewalls of the etched pillar (figure 7(c)) and by the Raman spectrum (figure 7(d)).

5. Conclusion

We studied the use of focused He and Ne beams to mill nanostructures in $BaTiO_3$ single crystals. Due to the low sputtering rate of $BaTiO_3$ with He ions, high doses are required to shape nanopillars, which result in a high concentration of He atoms in the crystal and eventually lead to surface blistering. Ne ion milling is found to be suitable for the fabrication of nanopillars of submicrometric dimensions. The ablation yield increases linearly with fluence. The lowest ion-induced structural damage is evidenced for the milling with 15 keV beams. We find a strong influence of the RPS on the shape of the pillars and on the induced damage. Cylindrical nanostructures with relatively low damage are most effectively achieved using the out–in RPS, whereas the in–out RPS and alternating RPS lead to an increased structural damage and deterioration of the cylindrical pillar geometry. HF acid proves to be efficient to remove the amorphized shell region, thus leading to a single crystalline nanopillar. Pillars with diameters down to ~80 nm can be achieved.

Ne ion milling is thus shown to be a suitable method for fast and efficient fabrication of $BaTiO_3$ nanostructures in single crystals. The method will be applied, in the future, to the realization of ferroelectric nanostructures in epitaxial films.

More generally, with this work, Ne ion milling appears as a precise machining tool for the fabrication of a large variety of complex oxide nanostructures—with desired shapes and dimensions—to explore diverse functional properties at the nanoscale. This micromachining method could also be used for the rapid prototyping of oxide nanodevices.

Acknowledgments

C D, V D, D J K, I I O, S W S acknowledge funding of the DFG and S S C, N C R C, J GF and CM acknowledge funding of the Agence Nationale de la Recherche in the framework of the bilateral DFG/ANR project FEAT (DFG 431399790/ANR-19-CE24-0027-01). CD, VD, DJK, IIO, SWS acknowledge the Corelab for Correlative Microscopy and Spectroscopy of the Helmholtz-Zentrum Berlin with the support of Holger Kropf, Victor Deinhaart and Katja Höflich.

Data availability statement

The data that support the findings of this study are available from the corresponding author upon reasonable request.

ORCID iDs

I I Olaniyan https://orcid.org/0009-0005-6843-0116
J Garcia Fernandez https://orcid.org/0000-0001-6136-3858
N Cherkashin https://orcid.org/0000-0002-0322-0864
S Schamm-Chardon https://orcid.org/0000-0001-5534-8475
C Dubourdieu https://orcid.org/0000-0002-4642-6897

References

[1] Ahn C H, Rabe K M and Triscone J M 2004 Ferroelectricity at the nanoscale: local polarization in oxide thin films and heterostructures *Science* **303** 488
[2] Scott J F 2007 Applications of modern ferroelectrics *Science* **315** 954

[3] Dubourdieu C *et al* 2013 Switching of ferroelectric polarization in epitaxial $BaTiO_3$ films on silicon without a conducting bottom electrode *Nat. Nanotechnol.* **8** 748

[4] Ihlefeld J F, Harris D T, Keech R, Jones J L, Maria J P and Trolier-McKinstry S 2016 Scaling effects in perovskite ferroelectrics: fundamental limits and process-structure-property relations *J. Am. Ceram. Soc.* **99** 2537

[5] Martin L W and Rappe A M 2016 Thin-film ferroelectric materials and their applications *Nat. Rev. Mater.* **2** 16087

[6] Yang S M, Morozovska A N, Kumar R, Eliseev E A, Cao Y, Mazet L, Balke N, Jesse S, Vasudevan R K and Dubourdieu C 2017 Mixed electrochemical–ferroelectric states in nanoscale ferroelectrics *Nat. Phys.* **13** 812

[7] Kelley K P *et al* 2022 Oxygen vacancy injection as a pathway to enhancing electromechanical response in ferroelectrics *Adv. Mater.* **34** 2016426

[8] McQuaid R G P, McGilly L J, Sharma P, Gruverman A and Gregg J M 2011 Mesoscale flux-closure domain formation in single-crystal $BaTiO_3$ *Nat. Commun.* **2** 404

[9] Zhang Q, Xie L, Liu G, Prokhorenko S, Nahas Y, Pan X, Bellaiche L, Gruverman A and Valanoor N 2017 Nanoscale bubble domains and topological transitions in ultrathin ferroelectric films *Adv. Mater.* **29** 1702375

[10] Yadav A K *et al* 2016 Observation of polar vortices in oxide superlattices *Nature* **530** 198

[11] Das S *et al* 2019 Observation of room-temperature polar skyrmions *Nature* **568** 368

[12] Tikhonov Y, Kondovych S, Mangeri J, Pavlenko M, Baudry L, Sené A, Galda A, Nakhmanson S, Heinonen O and Razumnaya A 2020 Controllable skyrmion chirality in ferroelectrics *Sci. Rep.* **10** 8657

[13] Luk'yanchuk I, Tikhonov Y, Sene A, Razumnaya A and Vinokur V M 2019 Harnessing ferroelectric domains for negative capacitance *Commun. Phys.* **2** 22

[14] Martelli P-W, Mefire S M and Luk'yanchuk I A 2015 Multidomain switching in the ferroelectric nanodots *Europhys. Lett.* **111** 50001

[15] Tan S, Livengood R, Shima D, Notte J and McVey S 2010 Gas field ion source and liquid metal ion source charged particle material interaction study for semiconductor nanomachining applications *J. Vac. Sci. Technol.*B **28** C6F15

[16] Bruchhaus L, Mazarov P, Bischoff L, Gierak J, Wieck A D and Hövel H 2017 Comparison of technologies for nano device prototyping with a special focus on ion beams: a review *Appl. Phys. Rev.* **4** 11302

[17] Li J and Liu Z 2018 Focused-ion-beam-based nano-kirigami: from art to photonics *Nanophotonics* **7** 1637

[18] Ganpule C S, Stanishevsky A, Aggarwal S, Melngailis J, Williams E, Ramesh R, Joshi V and Paz De Araujo C 1999 Scaling of ferroelectric and piezoelectric properties in $Pt/SrBi_2Ta_2O_9/Pt$ thin films *Appl. Phys. Lett.* **75** 3874

[19] Nagarajan V *et al* 2002 Realizing intrinsic piezoresponse in epitaxial submicron lead zirconate titanate capacitors on Si *Appl. Phys. Lett.* **81** 4215

[20] Saad M M, Bowman R M and Gregg J M 2004 Characteristics of single crystal 'thin film' capacitor structures made using a focused ion beam microscope *Appl. Phys. Lett.* **84** 1159

[21] Schilling A, Adams T B, Bowman R M, Gregg J M, Catalan G and Scott J F 2006 Scaling of domain periodicity with thickness measured in $BaTiO_3$ single crystal lamellae and comparison with other ferroics *Phys. Rev.*B **74** 24115

[22] McGilly L J, Schilling A and Gregg J M 2010 Domain bundle boundaries in single crystal $BaTiO_3$ lamellae: searching for naturally forming dipole flux-closure/quadrupole chains *Nano Lett.* **10** 4200

[23] Jia C L, Urban K W, Alexe M, Hesse D and Vrejoiu I 2011 Direct observation of continuous electric dipole rotation in flux-closure domains in ferroelectric $Pb(Zr, Ti)O_3$ *Science* **331** 1420

[24] Burns S R, Gregg J M and Nagarajan V 2016 Nanostructuring ferroelectrics via focused ion beam methodologies *Adv. Funct. Mater.* **26** 8367

[25] Stanishevsky A, Nagaraj B, Melngailis J, Ramesh R, Khriachtchev L and McDaniel E 2002 Radiation damage and its recovery in focused ion beam fabricated ferroelectric capacitors *J. Appl. Phys.* **92** 3275

[26] Schilling A, Adams T, Bowman R M and Gregg J M 2007 Strategies for gallium removal after focused ion beam patterning of ferroelectric oxide nanostructures *Nanotechnology* **18** 035301

[27] Hambe M, Wicks S, Gregg J M and Nagarajan V 2008 Creation of damage-free ferroelectric nanostructures via focused ion beam milling *Nanotechnology* **19** 175302

[28] Rahman F H M, McVey S, Farkas L, Notte J A, Tan S and Livengood R H 2012 The prospects of a subnanometer focused neon ion beam *Scanning* **34** 129

[29] Xia D, Zhu X, Khanom F and Runt D 2020 Neon and helium focused ion beam etching of resist patterns *Nanotechnology* **31** 475301

[30] Hayashi T, Arima K, Yamashita N, Park S, Ma Z, Tabata O and Kawai K 2018 Nanopore fabrication of two-dimensional materials on SiO_2 membranes using He Ion microscopy *IEEE Trans. Nanotechnol.* **17** 727

[31] Deng Y, Wang G, Qiu Y, He D, Lin J and He J 2020 Nano-patterning of a monolayer molybdenum disulfide with sub-nanometer helium ion beam: considering its shape, size and damage *Nanotechnology* **31** 345302

[32] Yang J, Ferranti D C, Stern L A, Sanford C A, Huang J, Ren Z, Qin L-C and Hall A R 2011 Rapid and precise scanning helium ion microscope milling of solid-state nanopores for biomolecule detection *Nanotechnology* **22** 285310

[33] Zhang L, Heinig N F, Bazargan S, Abd-Ellah M, Moghimi N and Leung K T 2015 Direct-write three-dimensional nanofabrication of nanopyramids and nanocones on Si by nanotumefaction using a helium ion microscope *Nanotechnology* **26** 255303

[34] Deinhart V, Kern L-M, Kirchhof J N, Juergensen S, Sturm J, Krauss E, Feichtner T, Kovalchuk S, Schneider M and Engel D 2021 The patterning toolbox FIB-o-mat: exploiting the full potential of focused helium ions for nanofabrication *Beilstein J. Nanotechnol.* **12** 304

[35] Scholder O, Jefimovs K, Shorubalko I, Hafner C, Sennhauser U and Bona G-L 2013 Helium focused ion beam fabricated plasmonic antennas with sub-5 nm gaps *Nanotechnology* **24** 395301

[36] Gozar A, Litombe N E, Hoffman J E and Bozovic I 2017 Optical nanoscopy of high T_c cuprate nanoconstriction devices patterned by helium ion beams *Nano Lett.* **17** 1582

[37] Xia D, Jiang Y-B, Notte J and Runt D 2021 GaAs milling with neon focused ion beam: comparison with gallium focused ion beam milling and subsurface damage analysis *Appl. Surf. Sci.* **538** 147922

[38] El-Atwani O, Huynh C and Norris S 2016 Utilizing neon ion microscope for GaSb nanopatterning studies: nanostructure formation and comparison with low energy nanopatterning *Appl. Surf. Sci.* **370** 557

[39] Allen F I, Velez N R, Thayer R C, Patel N H, Jones M A, Meyers G F and Minor A M 2019 Gallium, neon and helium focused ion beam milling of thin films demonstrated for polymeric materials: study of implantation artifacts *Nanoscale* **11** 1403

[40] Pekin T C, Allen F I and Minor A M 2016 Evaluation of neon focused ion beam milling for TEM sample preparation *J. Microsc.* **264** 59

[41] Ziegler J F and Biersack J P 1985 The stopping and range of ions in matter *Treatise Heavy-Ion Sci.* 6 (Springer) 93

[42] Veligura V, Hlawacek G, Berkelaar R P, van Gastel R, Zandvliet H J W and Poelsema B 2013 Digging gold: keV He+ ion interaction with Au *Beilstein J. Nanotechnol.* **4** 453
[43] Barrat J 2018 Helium and neon ion milling of β-Ga_2O_3 nanostructures *Bachelor Thesis* Humboldt Universität zu Berlin 17
[44] St-Jacques R G, Veilleux G, Martel J G and Terreault B 1980 Helium blistering of niobium: large swelling measurements supporting the gas pressure model *Radiat. Eff.* **47** 233
[45] Terreault B, Ross G, St.-Jacques R G and Veilleux G 1980 Evidence that helium irradiation blisters contain high-pressure gas *J. Appl. Phys.* **51** 1491
[46] Marshall M M, Yang J and Hall A R 2012 Direct and transmission milling of suspended silicon nitride membranes with a focused helium ion beam *Scanning* **34** 101
[47] Cerofolini G F, Corni F, Frabboni S, Nobili C, Ottaviani G and Tonini R 2000 Hydrogen and helium bubbles in silicon *Mater. Sci. Eng. R Reports* **27** 1
[48] Evans J H 1977 An interbubble fracture mechanism of blister formation on helium-irradiated metals *J. Nucl. Mater.* **68** 129
[49] Stanford M G, Lewis B B, Mahady K, Fowlkes J D and Rack P D 2017 Review Article: advanced nanoscale patterning and material synthesis with gas field helium and neon ion beams *J. Vac. Sci. Technol.* B **35** 030802
[50] Allen F I, Hosemann P and Balooch M 2020 Key mechanistic features of swelling and blistering of helium-ion-irradiated tungsten *Scr. Mater.* **178** 256
[51] Kato N I, Kohno Y and Saka H 1999 Side-wall damage in a transmission electron microscopy specimen of crystalline Si prepared by focused ion beam etching *J. Vac. Sci. Technol.*A **17** 1201
[52] Tanuj K, Ashish K, Dinesh C A, Nirnajan P L and Dinalar K 2013 Ion beam-generated surface ripples: new insight in the underlying mechanism *Nanoscale Res. Lett.* **8** 336
[53] Donnell S E O and Reinke P 2009 Characterization of focused-ion-beam induced defect structures in graphite for the future guided self-assembly of molecules *J. Vac. Sci. Technol.*B **27** 2209
[54] Park C M, Bain J A, Clinton T W, Van Der Heijden P A A and Klemmer T J 2004 Measurement of Ga implantation profiles in the sidewall and bottom of focused-ion-beam-etched structures *Appl. Phys. Lett.* **84** 3331
[55] Gajović A, Pleština J V, Žagar K, Plodinec M, Šturm S and Čeh M 2013 Temperature-dependent Raman spectroscopy of $BaTiO_3$ nanorods synthesized by using a template-assisted sol–gel procedure *J. Raman Spectrosc.* **44** 412
[56] Rubio-Marcos F, Campo A, Del, Marchet P and Fernández J F 2015 Ferroelectric domain wall motion induced by polarized light *Nat. Commun.* **6** 6594
[57] Dwij V, De B K, Sharma G, Shukla D K, Gupta M K, Mittal R and Sathe V 2022 Revisiting eigen displacements of tetragonal BaTiO3: Combined first principle and experimental investigation *Phys. B Condens. Matter.* **624** 413381
[58] Toulouse C *et al* 2021 Patterning enhanced tetragonality in $BiFeO_3$ thin films with effective negative pressure by helium implantation *Phys. Rev. Mater.* **5** 24404
[59] Guo H *et al* 2015 Strain doping: reversible single-axis control of a complex oxide lattice via helium implantation *Phys. Rev. Lett.* **114** 256801
[60] Herklotz A *et al* 2019 Designing morphotropic phase composition in $BiFeO_3$ *Nano Lett.* **19** 1033